Petroleum Science 21 (2024) 4219–4229

Contents lists available at ScienceDirect

Petroleum Science

journal homepage: www.keaipublishing.com/en/journals/petroleum-science

Original Paper

Study of the evolution characteristics of fiber-optic strain induced by the propagation of bedding fractures in hydraulic fracturing

Su Wang [a, b], Mian Chen [a, b, *], Jia-Xin Lv [a, b], Kun-Peng Zhang [c], Ya-Long Hao [a, b], Bo-Wen Yao [a, b]

[a] State Key Laboratory of Petroleum Resources and Engineering, China University of Petroleum (Beijing), Beijing, 102249, China
[b] Key Laboratory of Petroleum Engineering, Ministry of Education, China University of Petroleum (Beijing), Beijing, 102249, China
[c] Beijing International Center for Gas Hydrate, School of Earth and Space Sciences, Peking University, Beijing, 100871, China

ARTICLE INFO

Article history:
Received 19 December 2023
Received in revised form
9 September 2024
Accepted 10 September 2024
Available online 13 September 2024

Edited by Yan-Hua Sun

Keywords:
Distributed fiber-optic sensing
Identification of fracture growth
Shale reservoir
Bedding fractures
Fiber-optic strain

ABSTRACT

Shale reservoirs contain numerous bedding fractures, making the formation of complex fracture networks during fracturing a persistent technical challenge in evaluating shale fracture morphology. Distributed optical fiber sensing technology can effectively capture the process of fracture initiation and propagation, yet the evaluation method for the initiation and propagation of bedding fractures remains immature. This study integrates a distributed optical fiber sensing device based on optical frequency domain reflectometry (OFDR) with a large-scale true tri-axial fracturing physical simulation apparatus to conduct real-time monitoring experiments on shale samples from the Lianggaoshan Formation in the Sichuan Basin, where bedding is well-developed. The experimental results demonstrate that two bedding fractures in the shale sample initiated and propagated. The evolution characteristics of fiber-optic strain in a horizontal adjacent well, induced by the initiation and propagation of bedding fractures, are characterized by the appearance of a tensile strain convergence zone in the middle of the optical fiber, flanked by two compressive strain convergence zones. The initiation and propagation of the distal bedding fracture causes the fiber-optic strain in the horizontal adjacent well to superimpose, with the asymmetric propagation of the bedding fracture leading to an asymmetric tensile strain convergence zone in the optical fiber. Utilizing a finite element method coupled with a cohesive element approach, a forward model of fiber-optic strain in the horizontal adjacent well induced by the initiation and propagation of hydraulic fracturing bedding fractures was constructed. Numerical simulation analyses were conducted to evaluate the evolution of fiber-optic strain in the horizontal adjacent well, confirming the correctness of the observed evolution characteristics. The presence of a "wedge-shaped" tensile strain convergence zone in the fiber-optic strain waterfall plot, accompanied by two compressive strain convergence zones, indicates the initiation and propagation of bedding fractures during the fracturing process. These findings provide valuable insights for interpreting distributed fiber-optic data in shale fracturing field applications.

1. Introduction

Hydraulic fracturing is a crucial technology for enhancing reservoir permeability and increasing the production scale of oil and gas in shale development (Chang et al., 2022; Hou et al., 2021; Wei et al., 2022). However, the significant heterogeneity of shale reservoirs results in artificial fractures that intersect with bedding fractures and high-angle natural fractures during hydraulic fracturing, forming a complex fracture network. This complexity complicates the acquisition of accurate fracture parameters, leading to a lack of direct data for fracturing design (Chang and Hou, 2023; Hou et al., 2015). Therefore, accurately identifying the initiation and propagation of bedding fractures is essential for optimizing fracturing parameters in shale reservoirs (Lei et al., 2021; Hou et al., 2022a).

* Corresponding author. State Key Laboratory of Petroleum Resources and Engineering, China University of Petroleum (Beijing), Beijing, 102249, China.
E-mail address: chenm@cup.edu.cn (M. Chen).

https://doi.org/10.1016/j.petsci.2024.09.010

Real-time fracture monitoring technology is the primary method for evaluating fracture morphology. In recent years, on-site monitoring techniques have included microseismic monitoring, inclinometer monitoring, and distributed fiber optic sensing (Wei et al., 2021; Hou et al., 2019a; Zhang et al., 2021; Cippolla and Wright, 2002). Among these, distributed fiber optic sensing, the latest real-time fracture monitoring method, effectively captures the process of fracture propagation (Bassa et al., 2021; Hou et al., 2022b; Sui et al., 2021, 2023; Kavousi et al., 2017). Shell was the first to employ distributed acoustic sensing (DAS) technology to monitor the fracturing process of tight gas wells, proposing an effective method for identifying the propagation of multiple vertical fractures using fiber optic sensing (Molenaar et al., 2012). In the HFTS-2 experiment, three horizontal and one vertical fiber-optic wells were deployed, utilizing DAS, distributed temperature sensing (DTS), and distributed strain sensing via Rayleigh frequency shift (DSS-RFS) to estimate vertical fracture morphology through various fiber optic configurations (Bourne et al., 2021; Ciezobka, 2021; Gale et al., 2021; Ugueto et al., 2021). Furthermore, several scholars have conducted laboratory-based fiber optic fracturing experiments. Zhang et al. (2022) integrated a distributed fiber optic reflectometer based on optical frequency domain reflectometry (OFDR) with a large-scale true tri-axial fracturing simulation apparatus to perform hydraulic fracturing simulations on concrete specimens, determining the evolution of fiber-optic strain in adjacent wells induced by vertical fracture propagation. Wang et al. (2023) combined distributed fiber optic sensing with a clustered dynamic flow control experimental device to conduct multi-cluster hydraulic fracturing simulations, proposing a method to identify the characteristics of fiber-optic strain evolution induced by the propagation of multiple fractures.

While distributed optical fiber sensing technology has rapidly advanced, particularly in evaluating vertical fracture morphology, shale fracturing often involves not only the generation of vertical fractures but also the interaction with a multitude of bedding fractures, forming a complex fracture network (Shi et al., 2019; Zeng et al., 2022). Current evaluation methods, however, do not accurately assess the initiation and propagation of bedding fractures. In previous indoor physical simulation experiments, under simulated downhole geo-stress conditions, complex fracture patterns comprising orthogonal vertical fractures and bedding fractures were easily formed, but the fiber-optic data collected from these experiments could not accurately evaluate the fiber-optic strain responses induced by bedding fracture initiation and propagation. Similarly, existing numerical models for hydraulic fracturing have failed to accurately characterize the properties of beddings and the behavior of bedding fractures during their initiation and propagation. To address these challenges, this study integrates an OFDR-based distributed fiber-optic demodulator with large-scale true tri-axial fracturing physical simulation experiments, selecting shale outcrops with well-developed bedding fractures for preparation and wrapping to conduct indoor physical simulation experiments on horizontal well fracturing of shale samples monitored by horizontal adjacent wells using optical fibers. The strain data from these optical fibers are analyzed to elucidate the evolution of strain induced by the initiation and propagation of bedding fractures. This paper characterizes the nature of bedding fractures and their initiation and propagation behavior, constructing a numerical model to monitor these processes using optical fibers in horizontal adjacent wells. By analyzing the results of physical simulation experiments and forward simulations, the study verifies the accuracy of the observed strain evolution in optical fibers and proposes a method for detecting bedding fracture initiation and propagation based on distributed fiber-optic strain data. All bedding fractures mentioned in this paper refer to horizontal bedding fractures.

2. Distributed fiber optic hydraulic fracturing physical simulation experiment

2.1. Optical frequency domain reflectometry (OFDR) principle

The distributed fiber-optic demodulator used in this paper is based on OFDR, which detects events and failures in an optical fiber by analyzing the frequency changes of the light reflected or scattered back. The principle is as follows: OFDR sends a series of narrow pulses of light signals of different frequencies into the fiber, which are reflected by changes within the fiber (strain or temperature changes) as they propagate through the fiber, as shown in Eq. (1). These reflected signals are captured by the fiber and returned to the system. the OFDR analyzes the frequency characteristics of the received reflected signals and determines the location and nature of the changes in the fiber based on the frequency distribution of the signals. Finally, the system processes the data to generate images or data reflecting the strain or temperature changes in the fiber for analysis and monitoring purposes. In indoor physical simulation experiments of hydraulic fracturing, OFDR can be used to monitor the strain or temperature distribution along distributed optical fibers to infer the initiation and propagation of fractures.

$$\frac{\Delta\lambda}{\lambda}=\frac{-\Delta\nu}{\nu}=K_{\mathrm{e}}\varepsilon_{\mathrm{f}}+K_{\mathrm{T}}\Delta T \tag{1}$$

where λ represents the average wavelength, m; $\Delta\lambda$ represents the wavelength shift amount, m; ν represents the average optical frequency, Hz; $\Delta\nu$ represents the optical frequency shift, Hz; K_{e} represents the strain sensitivity factor, dimensionless; ε_{f} represents the fiber-optic strain, dimensionless; K_{T} represents the temperature sensitivity factor, K^{-1}; ΔT represents the amount of temperature change, K.

2.2. Experimental equipment

The experimental equipment consists of two main parts: distributed sensing fiber-optic data acquisition equipment and hydraulic fracturing physical simulation experimental equipment.

The distributed sensing fiber-optic data acquisition equipment consists of five parts (Fig. 1): (1) OSI-D dynamic fiber-optic data acquisition instrument. Equipped with a high-precision distributed fiber-optic sensing system, it collects fiber-optic signals based on OFDR. (2) Fiber-optic data processing computer. It converts the signals collected by the OSI-D dynamic host into strain signals of the distributed optical fiber. (3) Traction optical cable. Used for long-distance fiber monitoring, its length is 100 m. (4) Fiber optic guide box. Used to connect the traction optical cable and jumper. (5) Jumper. Used to connect the fiber sensing section with the fiber optic guide box. Among them, the static data acquisition spatial resolution of the OFDR demodulator can reach 1.28 mm, the strain measuring accuracy can reach $\pm1\mu\varepsilon$, and the sampling rate is 6 Hz. The sensing fiber used in this experiment is a bare fiber with a diameter of 125 μm, mainly used for monitoring strain information and transmitting data. The polyimide coating wrapped around the outside of the fiber is used to fix and protect the inner bare fiber. Through testing, it is known that its macro-bend loss is approximately 0 (Yan et al., 2014).

The physical simulation experiment of hydraulic fracturing uses a large-scale true tri-axial fracturing simulation system designed by the Rock Mechanics Laboratory of China University of Petroleum (Beijing). The initiating, turning, and propagation morphology of hydraulic fractures in the simulated wellbore are monitored by the

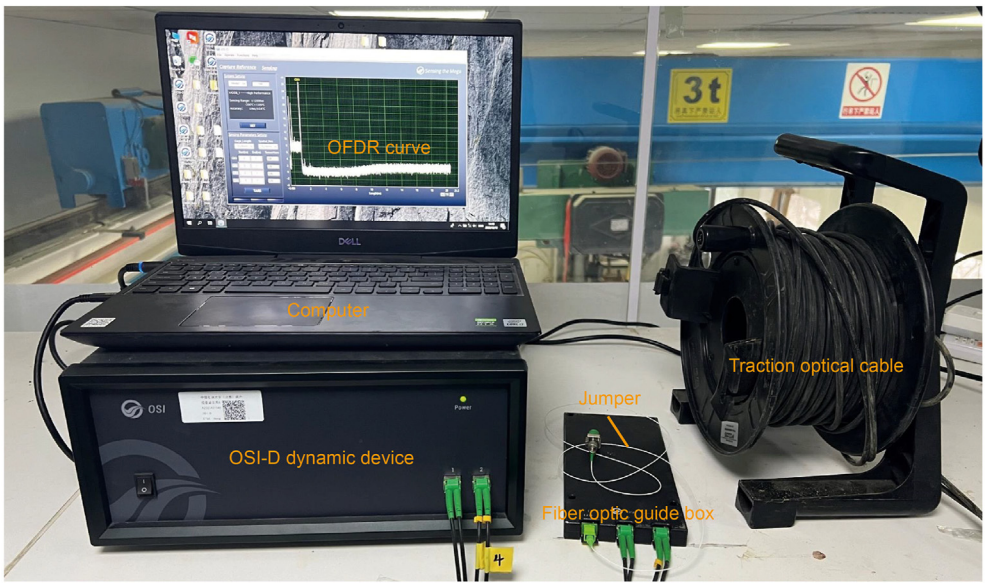

Fig. 1. Photo of optical fiber OSI-D dynamic equipment.

OFDR system (Hou et al., 2019b). The testing system consists of a true tri-axial experimental component, a tri-axial hydraulic stabilizing source (WY-300VIII), hydraulic fluid and hydraulic power oil isolation components, an MTS pressurization and controller, and a data acquisition and processing system (Fig. 2).

2.3. Sample preparation

Cut the shale outcrop into cubic shale samples with a side length of 200 mm. To insert the optical fiber, a U-shaped groove must be cut into the shale sample for positioning the optical fiber. Next, drill a wellbore in the center of the sample, sized to accommodate the wellbore insertion, using a water drill. After the sample is dried, adhere the optical fiber in the U-shaped groove using fiber optic adhesive. Once the adhesive is fully dried, test the optical fiber to ensure it is not damaged. If no issues are found, insert the wellbore into the drilled hole and perform well cementing using cementing adhesive. To ensure that the hydraulic fracturing true tri-axial experimental apparatus can apply confining pressure to the sample, wrap the shale sample with cement mortar to form a cubic sample with a side length of 300 mm. The tail reflection segment and jumper segment should not be fully embedded in the cement mortar, and the volume ratio of cement to quartz sand should be 1:1. The vertical section of the optical fiber is used to simulate the fiber optic in the horizontal adjacent well (Fig. 3).

After the casting of the specimen is completed, the specimen

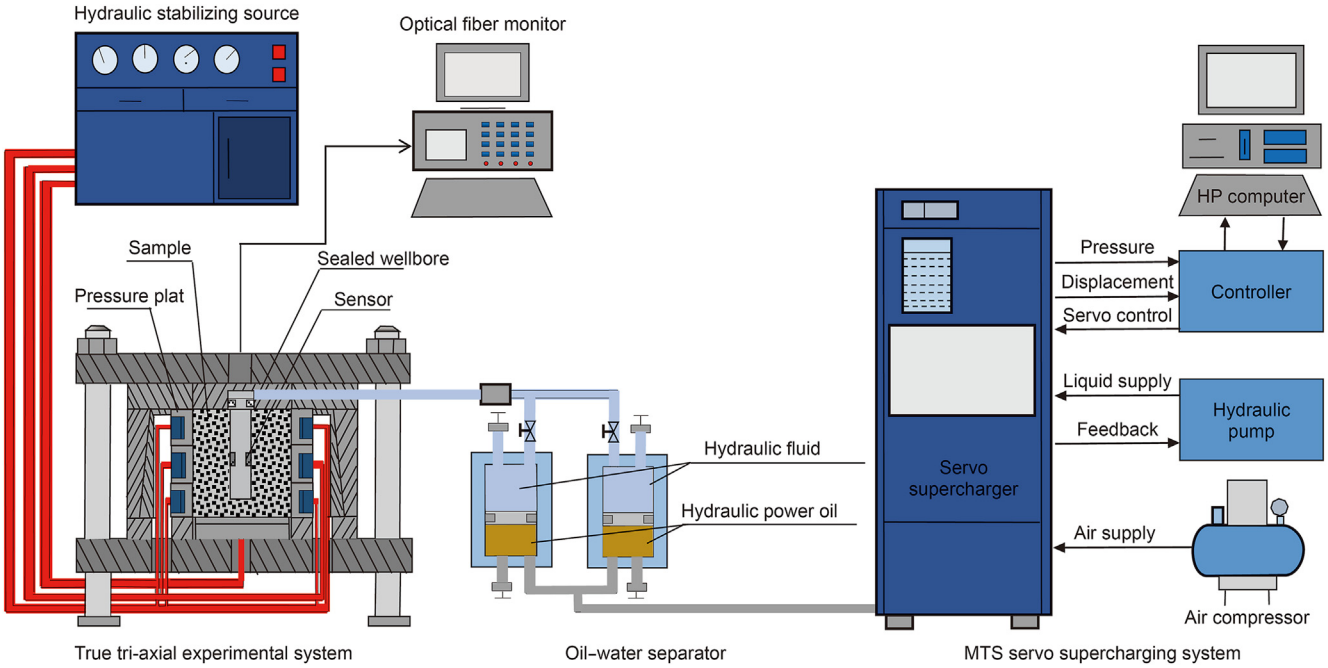

Fig. 2. Schematic plot of optical fiber monitoring true tri-axial fracturing experimental system.

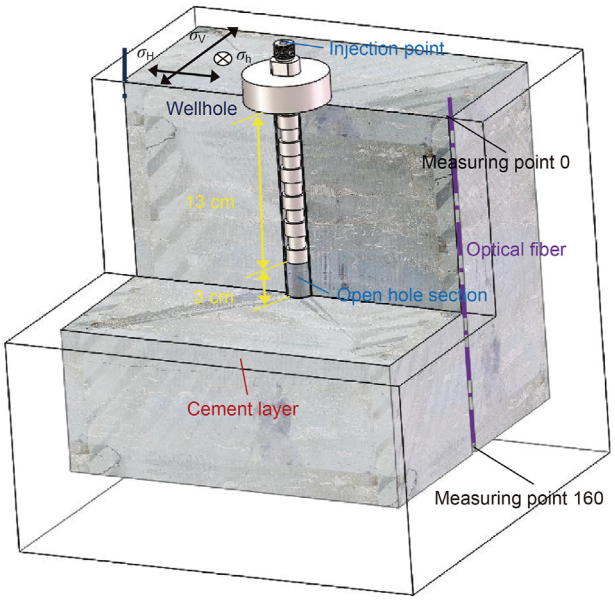

Fig. 3. Schematic diagram of shale fiber optic wiring mode and shale sample cement mortar wrapping.

should be placed for 30 days for curing and drying. Based on indoor testing experiments, the basic mechanical parameters of the shale specimen and the specimen after casting are obtained (Table 1).

2.4. Experimental steps

Experimental operating steps are as follows:

(i) Place the sample and install the confining pressure plate. Put the sample into the true tri-axial physical simulation test frame and install the flat jack pressure plate and confining pressure components. During this process, the jumper should be protected to avoid any breakage.
(ii) Connect the optical fiber to the fiber optic box. Use a fiber optic cleaner to clean the first end of the optical fiber and connect it to the fiber optic box, and check the integrity of the fiber optic sensing part.
(iii) Apply true tri-axial confining pressure. The confining pressure loading device applies tri-axial confining pressure to the sample to simulate the in-situ stress of the oil field. The test parameters are calculated based on the results of the in-situ stress test and similarity criteria (De Pater et al., 1994). The horizontal stress difference is set to 8 MPa, the maximum horizontal principal stress is set to 26 MPa, the minimum horizontal principal stress is set to 18 MPa, and the overburden stress is set to 28 MPa. After applying the confinement pressure, wait for about 30 min to ensure the balance of the confinement pressure.
(iv) Locate the sensing segment of the optical fiber. Use a fiber optic needle to dip a small amount of liquid nitrogen for fiber optic positioning, determine the sensing segment of the optical fiber, and record the starting point of the fiber optic sensing segment.
(v) Start fracturing and perform fiber optic monitoring. According to the set displacement, inject fluid into the wellbore through the injection system, start fracturing until the sample fractures, and stop pumping. The displacement is set to 30 mL/min. During this period, select the reference segment of the optical fiber, and turn on the fiber optic sensing device for real-time monitoring.
(vi) Save data and open the sample. Save the collected pump pressure curve and fiber-optic strain monitoring data in the experiment, open the sample along the hydraulic fracture, observe and record the starting position and propagation morphology of the fracture, and interpret the fiber-optic strain monitoring data. Fiber-optic strain data processed by wavelet de-noising method. The principle is as follows: using the multi-scale analysis characteristics of the wavelet transform, the signal is decomposed into sub-signals of different frequencies, and then some wavelet coefficients are adjusted or discarded to achieve the effect of noise reduction.

It should be noted that the fracturing fluid needs to be at the same temperature as the room temperature to eliminate the influence of temperature difference on the sensing optical fiber (Wang et al., 2023).

3. Experimental results and analysis

In order to monitor the initiation and propagation of bedding fractures and induce the evolution characteristics and laws of adjacent well fiber-optic strain, the experimental shale outcrop selected for this study is the Lianggaoshan Formation shale in the Sichuan Basin, which has well-developed bedding planes. The lithology of the Lianggaoshan Formation shale reservoir is complex, with mostly horizontal bedding planes. Moreover, there are multiple natural bedding plane fractures in the shale sample that meet

Fig. 4. The shale sample from Lianggaoshan Formation in Sichuan Basin.

Table 1
Basic mechanical parameters of the samples.

	Young's modulus, GPa	Poisson's ratio	Uniaxial tensile strength, MPa	Uniaxial compressive strength, MPa	Permeability, mD	Porosity, %
Shale	35.81	0.20	43.60	3.41	0.09	1.55
Sample after pouring	27.79	0.22	22.91	1.63	0.10	0.60

the experimental requirements (Fig. 4).

After fracturing, the sample is dissected, and two opening bedding fractures (BF1 and BF2 in Fig. 5) can be observed. There is a vertical fracture between BF1 and BF2, serving as a connecting channel. As shown in Fig. 5, BF1, which is closer to the optical fiber, is the first to initiate and propagate. As the fracturing progresses, some natural weak planes in the sample are activated, forming a vertical fracture that connects to BF2. BF2 exhibits asymmetric propagation.

Fig. 6 presents the strain waterfall plot and pump pressure curve of the vertical section of the fiber optic (horizontal adjacent well fiber optic) during the sample fracturing process. The strain waterfall plot illustrates the evolution of strain within the fiber optic. The horizontal axis represents the progression of the fracturing process along the axial direction. In the plot, "red" indicates tensile strain, while "blue" signifies compressive strain. The vertical sensing section of the fiber optic contains 160 measurement points in total. From Fig. 6(b), it can be observed that multiple pressure drops occur during the fracturing process. The first and last pressure drops are the most significant, corresponding to the initiation of bedding fractures BF1 and BF2, respectively. Between these two major pressure drops, multiple pressure fluctuations occur due to the activation of natural weak surfaces within the sample during fracturing.

Fig. 6(a) shows that the vertical section of the fiber optic barely detects any strain response induced by the activation of these natural weak surfaces. However, the initiation and propagation of the two bedding fractures produce a significant strain response in the vertical section of the fiber optic. The initiation and propagation of BF1 generate a gradually expanding tensile strain zone in the horizontal adjacent well fiber optic, with a small compressive strain zone appearing on the periphery of the tensile strain zone. The strain waterfall plot reveals a "wedge-shaped" tensile strain convergence band in the middle of the fiber optic, flanked by two compressive strain convergence bands that gradually extend outward. The initiation and propagation of BF2 further expand the range and magnitude of the tensile strain zone in the middle of the horizontal adjacent well fiber optic. Although the strain waterfall plot continues to show a "wedge-shaped" tensile strain convergence band in the middle of the optical fiber, the asymmetric propagation of BF2 results in an asymmetric "wedge-shaped" tensile strain convergence band.

In summary, the initiation and propagation of the bedding fractures induce the following horizontal adjacent fiber-optic strain response characteristics: a gradually expanding tensile strain zone appears in the middle, and a small range of compressive strain zone appears on the outside of this tensile strain zone; in the strain waterfall plot, a "wedge-shaped" tensile strain convergence zone appears in the middle, and outside of this convergence zone, there are 2 gradually outward expanding compressive strain convergence zones. The asymmetric expansion of the bedding fractures will cause the "wedge-shaped" tensile strain convergence zone to be asymmetric.

4. Verification of forward numerical models

4.1. Model summary

The generation of fractures leads to a redistribution of the strain field within the strata, causing the fiber optic located at the far end of the strata to experience strain. Assuming that there is no transmission loss of strain from the strata to the fiber optic, the fiber-optic strain can be regarded as equivalent to the strata strain (Chen et al., 2022). In this study, the fiber optic monitoring well is set as a horizontal well, with the fiber optic monitoring the axial strain along its length. A bedding plane parallel to the fiber optic is established, and the following assumptions are made: (1) The strata are uniform and isotropic. (2) The fracturing process is quasi-static. (3) The displacement during the fracturing process remains constant. (4) The effect of friction is not considered. (5) Bedding fractures propagate exclusively within the bedding plane.

4.2. Model building

This article uses cohesive elements to simulate fracture damage and fracture processes, and the damage evolution is based on displacement criteria (Lv et al., 2021). Before damage occurs, the stress–strain relationship follows the linear elastic relationship. When the stress increases to the ultimate strength, the rock undergoes damage. The maximum stress initiation criterion is used to describe the initiation behavior of hydraulic fractures. This criterion states that when the stress in any direction reaches the critical stress for unit damage, the unit will undergo damage, as shown in Eq. (2).

$$\max\left\{\frac{\sigma_n}{\sigma_n^0}, \frac{\sigma_s}{\sigma_s^0}, \frac{\sigma_t}{\sigma_t^0}\right\} = 1 \tag{2}$$

where σ_n represents the stress in the normal direction, Pa; σ_s, σ_t

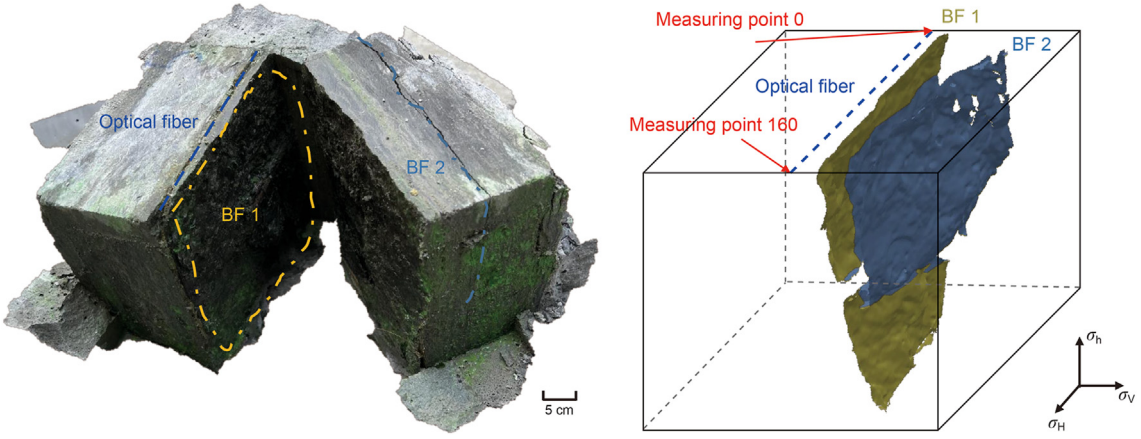

Fig. 5. Fracture propagation morphology of shale samples after fracturing (BF1 is bedding fracture 1, BF2 is bedding fracture 2).

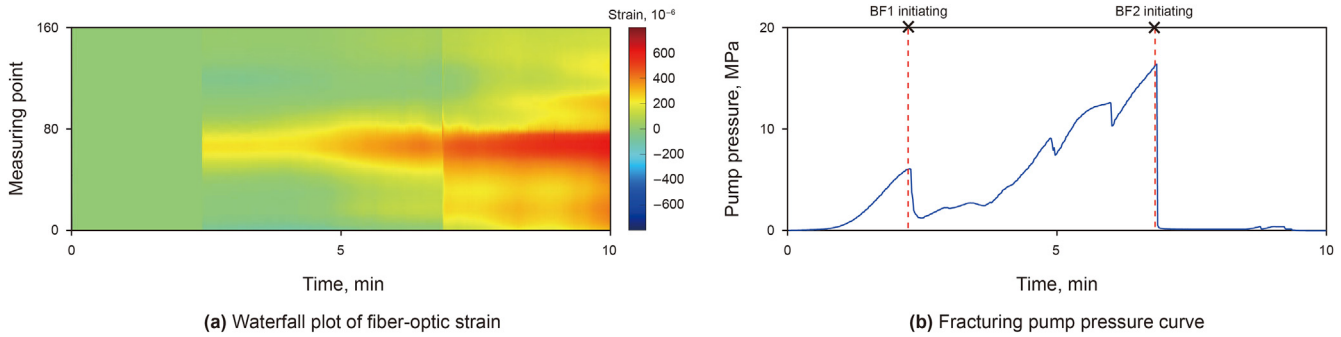

(a) Waterfall plot of fiber-optic strain **(b)** Fracturing pump pressure curve

Fig. 6. Fiber-optic strain waterfall plot and pump pressure curve for sample fracturing.

represent the stresses in the tangential direction, Pa; σ_n^0 represents the critical stress in the normal direction, Pa; σ_s^0, σ_t^0 represent the critical stresses in the tangential direction, Pa.

The unit is damaged when subjected to tension, but not when subjected to pressure, as shown in Eq. (3).

$$\langle \sigma_n \rangle = \begin{cases} \sigma_n & \sigma_n \geq 0 \\ 0 & \sigma_n \leq 0 \end{cases} \tag{3}$$

The expansion of hydraulic fractures is based on the damage evolution criterion of effective displacement, as shown in Eq. (4).

$$D = \frac{d_m^f \left(d_m^{max} - d_m^0 \right)}{d_m^{max} \left(d_m^f - d_m^0 \right)} \tag{4}$$

where D represents the damage variable, dimensionless; d_m^0 represents the displacement when damage occurs to the cohesive unit, m; d_m^{max} represents the maximum displacement of the cohesive unit during the damage process, m; d_m^f represents the displacement when the cohesive unit is completely destroyed, m.

Considering shale as an isotropic poro-elasticity solid (Wei et al., 2021), the strain ε and stress field σ of the forward model can be expressed as follows:

$$\varepsilon = \boldsymbol{B} u_e, \quad \sigma = \boldsymbol{K} \varepsilon = \boldsymbol{K} \boldsymbol{B} u_e \tag{5}$$

where $\boldsymbol{B}$ represents the derivative matrix, m^{-1}; u_e represents the nodal displacement, m; $\boldsymbol{K}$ represents the stiffness matrix, MPa.

Based on the relationship between displacement and strain, using the central difference method, the strain at the measuring point can be calculated based on the displacement at the measuring point.

$$\varepsilon_f = \frac{u_f(y + L/2) - u_f(y - L/2)}{L} \tag{6}$$

where ε_f represents the fiber-optic strain, dimensionless; u_f represents the axial displacement of the optical fiber, m; L represents the distance between fiber optic measuring points, m; y represents the coordinate value in the y direction of the location of the fiber optic measuring point, m.

Based on the method mentioned above, a forward model of hydraulic fracturing to induce horizontal adjacent well fiber-optic strain is established, as shown in Fig. 7. The length in the x direction of the model is 400 m, the length in the y direction is 400 m, and the length in the z direction is 200 m. The bedding plane is set at $z = 0$ m. The length of the fiber optic is 400 m, and the spacing between measuring points is 5 m. The distance between the optical fiber and the model boundary is h_x, and the distance between the

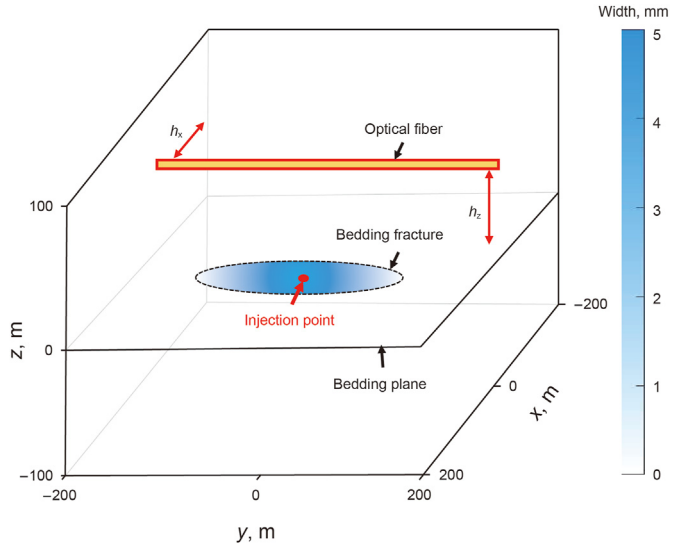

Fig. 7. Schematic diagram of distributed fiber optic monitoring hydraulic fracture forward model.

optical fiber and the bedding plane is h_z. The injection point is (0,0,0). The fracturing fluid only flows in the bedding plane, and the bedding fracture only propagates in the bedding plane.

4.3. Process of calculation

The main hydraulic fracturing model consists of three stages: the stage of fracturing fluid entering the perforation location, the stage of fracture propagation, and the stage of fracture propagation inducing optical fiber strain evolution. Initially, the fracturing fluid flows into the perforation location from the wellbore's starting point, activating cohesive force units that initiate and propagate fractures. The evolution of optical fiber strain in the horizontal adjacent well is then calculated based on the changes in the strain field caused by the initiation and propagation of hydraulic fractures. The calculation process is illustrated in Fig. 8.

4.4. Model setup

The geo-mechanical parameters for the model are shown in Table 2. The viscosity of the fracturing fluid is 5 mPa s, and the filtration loss coefficient is 1×10^{-4} m/min$^{0.5}$. The overlying stress of the model is set to 45 MPa, with the maximum and minimum horizontal principal stress values set to 50 and 40 MPa, respectively, and the displacement set to 1.2 m^3/min. The pumping time is

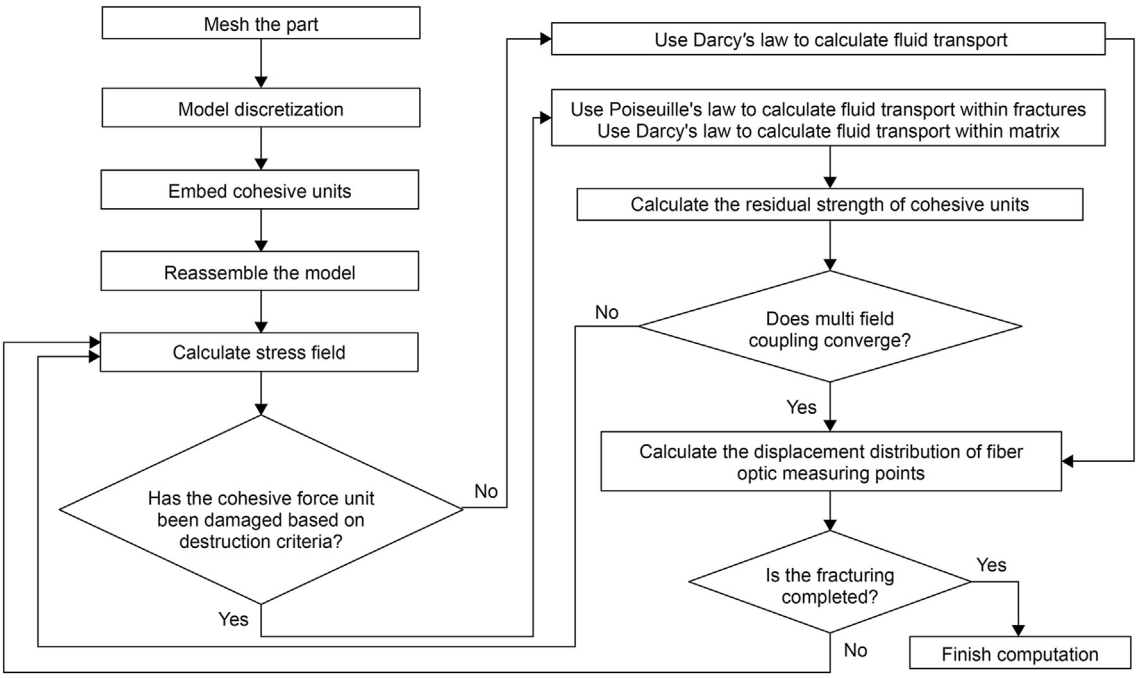

Fig. 8. Flow chart of forward modeling calculation for fiber-optic strain.

Table 2
The geo-mechanical parameters for the model.

Young's modulus, GPa	Poisson's ratio	Critical stress for cohesive elements failure, MPa	Permeability, mD	Porosity, %
28.00	0.25	10.00	0.10	1.55

60 min. The value of h_x is set to 150 m.

4.5. Results of calculation

The value of h_z is set to 150 m. The calculated result of the half-length of the fracture is shown in Fig. 9. When the construction time is 33 min, the half-length of the fracture reaches 75 m; the final fracture half-length of the fracturing construction is 85 m.

The calculated results of fiber-optic strain are shown in Fig. 10.

To further analyze the dynamic evolution of fiber-optic strain, three fiber-optic measurement points ($y = 0$, $y = 50$ m, and $y = 100$ m) were selected to examine the relationship between strain and fracturing time (Fig. 10(b)). It can be observed that as fracturing progresses, the strain at measurement point $y = 0$ steadily increases. When the fracturing time reaches the onset of the strain divergence stage, the strain begins to decrease, and the strain rate at the end of each stage undergoes changes. The strain at measurement points $y = 50$ m and $y = 100$ m initially decreases and then increases as fracturing continues. At 28 min, the strain at $y = 50$ m transitions from compressive to tensile, indicating the ongoing divergence of the "wedge-shaped" fiber-optic tensile strain signal. The strain at $y = 100$ m remains compressive, indicating that the outer side of the "wedge-shaped" fiber-optic tensile strain convergence zone is a compressive strain convergence zone.

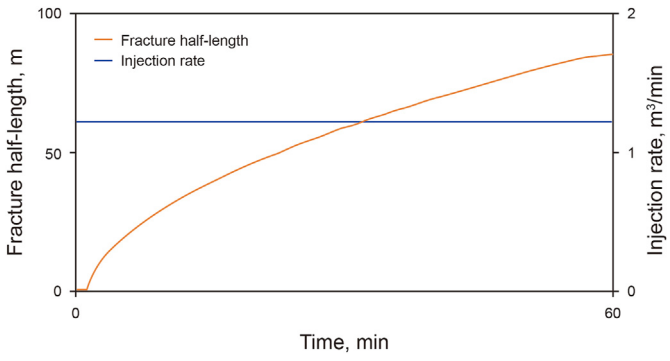

Fig. 9. The variation of fracture half-length with fracturing time.

When the distance between the optical fiber and the bedding plane (h_z) is 30, 70, and 90 m, the calculated fiber-optic strain results are shown in Fig. 11. It can be observed that within the effective monitoring range of the optical fiber, the farther the bedding fracture is from the optical fiber, the weaker the strain signal received. However, regardless of the distance, the evolution of fiber-optic strain induced by the initiation and propagation of the bedding fracture follows three stages: strain-enhancing, strain-converging, and strain-diverging. The initiation and propagation of the bedding fracture can trigger a "wedge-shaped" tensile strain convergence zone in the fiber-optic strain waterfall plot of the horizontal adjacent well, with two compressive strain convergence zones on the outer sides. In conclusion, within the effective monitoring range, the initiation and propagation of the bedding fracture can induce strain-enhancing, strain-converging, and strain-diverging stages in the optical fiber parallel to its spatial position. If a "wedge-shaped" tensile strain band appears in the fiber-optic strain waterfall plot, it may indicate the initiation and propagation of a bedding fracture parallel to that fiber position, and the distance to the bedding fracture can be inferred from the

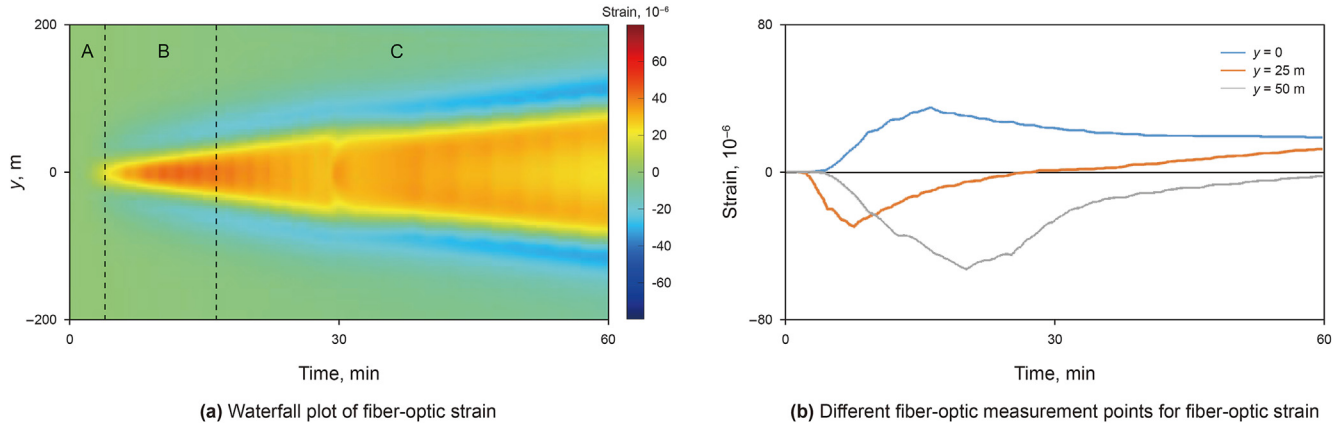

(a) Waterfall plot of fiber-optic strain **(b)** Different fiber-optic measurement points for fiber-optic strain

Fig. 10. Horizontal adjacent well fiber-optic strain calculation results (h_z = 50 m).

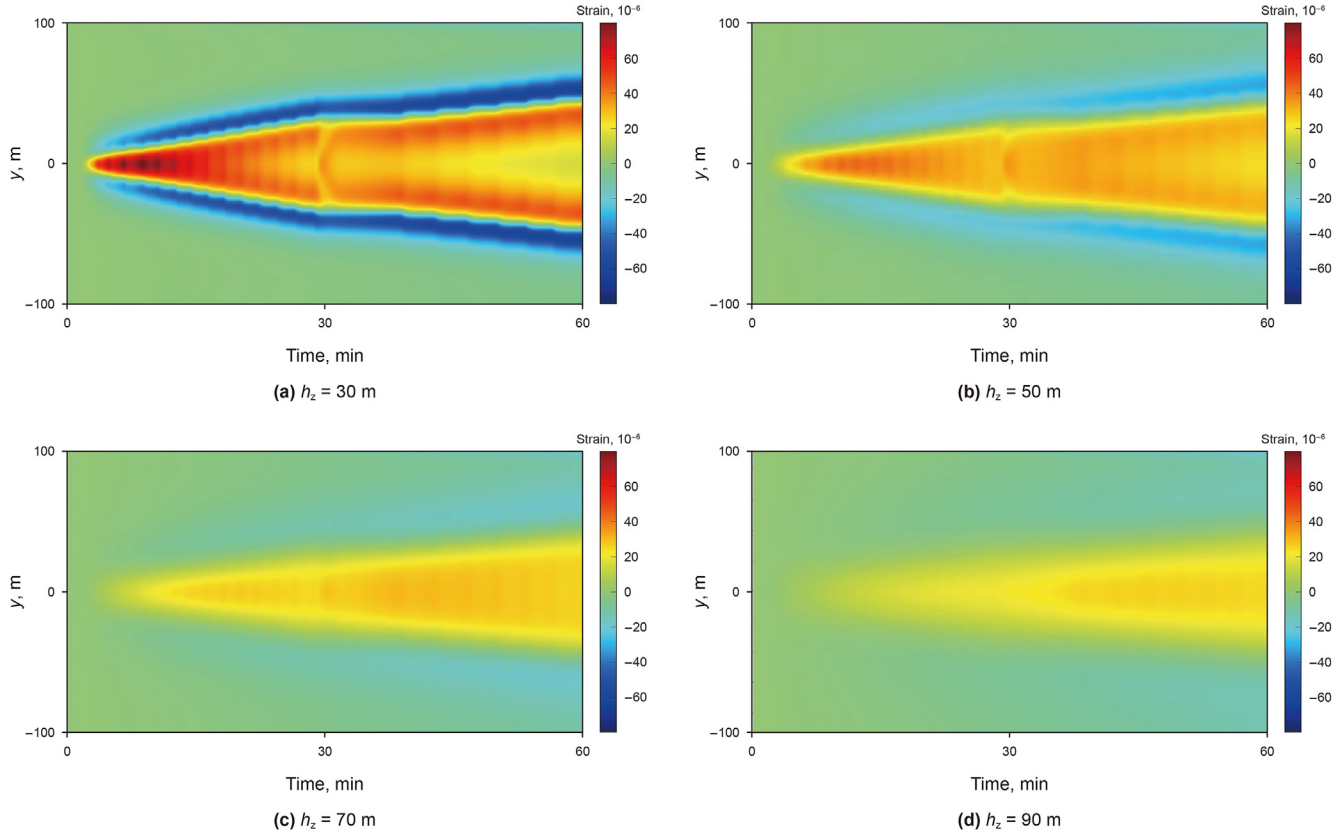

(a) h_z = 30 m **(b)** h_z = 50 m

(c) h_z = 70 m **(d)** h_z = 90 m

Fig. 11. Waterfall plot of fiber-optic strain at different distances between optical fibers and bedding plane.

strength of the fiber-optic strain signal received by the horizontal adjacent well.

4.6. Verification and discussion of fiber-optic strain evolution characteristics

The comparison between the results of physical simulation experiments and forward model calculations is shown in Fig. 12. It can be observed that the expansion of the bedding fracture in both numerical simulations and experiments induces three stages of fiber-optic strain evolution in the horizontal adjacent well: strain-enhancing stage (region A in Fig. 12(a) and (b)), strain-converging stage (region B in Fig. 12(a) and (b)), and strain-diverging stage (region C in Fig. 12(a) and (b)). The characteristics of strain evolution in the horizontal adjacent well optical fibers, induced by the initiation and propagation of the bedding fracture in the forward modeling, are as follows: a tensile strain convergence zone appears in the middle of the optical fiber, and two compressive strain convergence zones appear on both sides. In the strain waterfall plot, the middle section of the optical fiber shows a "wedge-shaped" tensile strain convergence zone, with two compressive strain convergence zones on the outer sides that gradually expand outward. These characteristics are similar to those observed in the fiber-optic strain evolution in the horizontal adjacent well obtained from forward modeling, except that the tensile strain convergence zone in the experimental results exhibits an asymmetrical

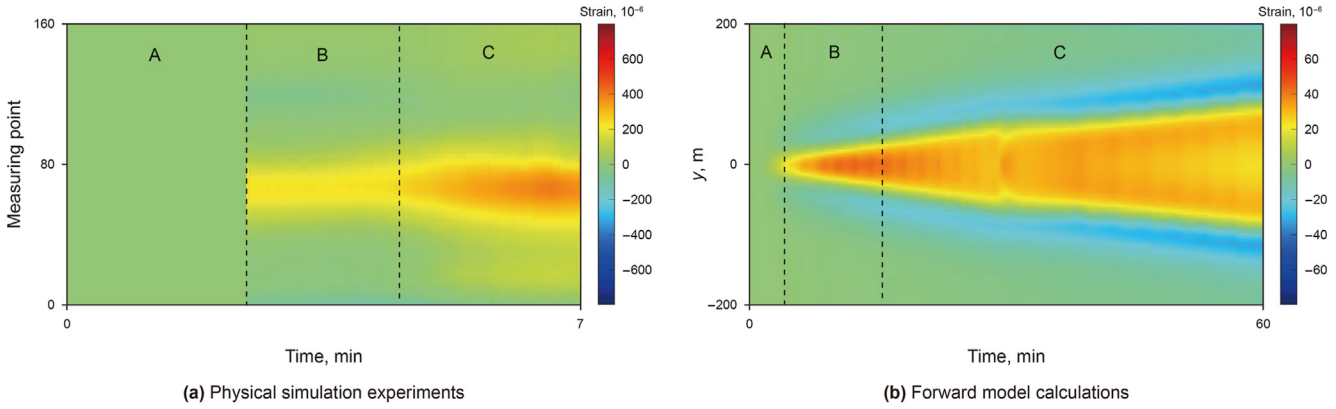

Fig. 12. Comparison of results between physical simulation experiments and forward model simulations.

phenomenon. This asymmetry is caused by the heterogeneity of the shale, leading to asymmetrical fracture propagation. Comparative analysis demonstrates the accuracy of the evolution patterns and characteristics of strain in the horizontal adjacent well optical fibers induced by the initiation and propagation of the bedding fracture as described above.

Based on the fracture propagation results obtained from the physical simulation experiments, this paper establishes a forward model of hydraulic fracturing 2-bedding fractures initiation and propagation induced fiber-optic strain in horizontal adjacent wells (Fig. 13). The geometry, geo-mechanical parameters and construction parameters of the model are the same as those of the previously described forward model. The distances between the optical fiber and the bedding planes are 50 and 70 m. The bedding plane that are farther away from the optical fiber are communicated when the pumping progresses to 28 min.

The calculated results of fiber-optic strain are shown in Fig. 14(a).

It can be seen that the strain evolution of the horizontal adjacent fiber induced by the initiation and propagation of the two bedding fractures is similar to the superposition of the strains induced by the two bedding fractures. The propagation of the second open bedding fracture expands the tensile strain zone in the middle of the horizontal adjacent well fiber, and the strain value becomes larger, and the strain waterfall plot still shows a "wedge-shaped" tensile strain convergence zone in the middle of the optical fiber. Comparing the results of the physical simulation and the forward model (Fig. 14), it can be seen that the initiation and propagation of multiple bedding fractures will lead to the superposition of the fiber-optic strains, and the initiation and propagation of each bedding fracture will lead to the emergence of a "wedge-shaped" tensile-strain convergence zone in the horizontal adjacent well fiber. According to the characteristics of the evolution of strain in horizontal adjacent wells optical fibers induced by the initiation and propagation of bedding fractures, it can be known that if there is a "wedge-shaped" strain aggregation zone in the waterfall plot of strain in adjacent wells, and there are two gradually expanding compression strain aggregation zones on the outside of the aggregation zone, it indicates the initiation and extension of bedding fractures during the hydraulic fracturing process. The symmetry of the extension of bedding fractures can be determined based on whether the "wedge-shaped" strain aggregation zone is symmetrical, and this can guide the design of hydraulic fracturing construction parameters.

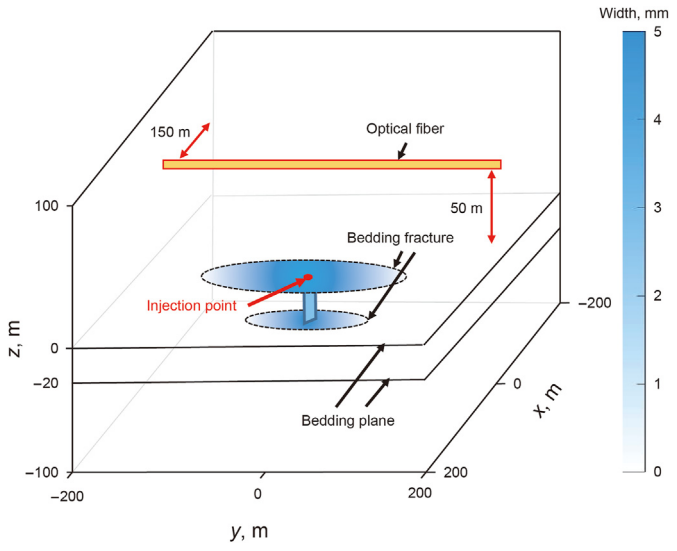

Fig. 13. Schematic diagram of distributed fiber optic monitoring 2-bedding fractures forward model.

5. Conclusions

This article applies distributed fiber-optic strain sensing technology to evaluate the initiation and propagation status of bedding fractures. A series of exploratory studies combining distributed optical fiber monitoring technology with hydraulic fracturing indoor physical simulation experiments has been conducted. The finite element coupled cohesive force element method is applied for numerical simulation verification. The main conclusions are as follows:

(1) The initiation and propagation of bedding fractures induce strain evolution in horizontal adjacent well optical fibers, which can be divided into three stages: strain-enhancing, strain-converging, and strain-diverging stage; the characteristic of strain evolution is the appearance of a tension strain convergence zone in the middle of the optical fiber and two compression strain convergence zones on both sides.
(2) In the distributed fiber-optic strain waterfall plot of horizontal adjacent wells, a "wedge-shaped" strain convergence zone appears, and there are two gradually expanding compressive strain convergence zones on the outer side of the convergence zone, indicating the possible initiation and expansion of bedding plane fractures.

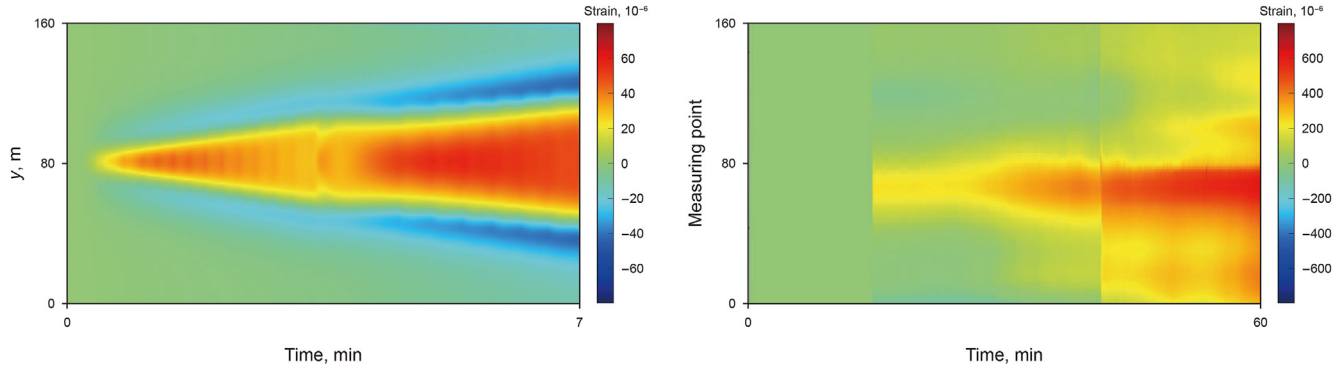

(a) Forward model calculations of 2-bedding fractures

(b) Physical simulation experiments

Fig. 14. Comparing the results of the physical simulation and the forward model.

(3) The initiation and propagation of multiple bedding fractures can lead to the superposition of fiber-optic strain in horizontal adjacent wells. The asymmetric extension of the bedding fracture leads to the asymmetry of the tensile strain convergence band in the middle of the optical fiber. The symmetry of the bedding fracture propagation can be determined based on whether the convergence band is symmetrical.

(4) The forward modeling of adjacent well fiber-optic strain induced by hydraulic fracture propagation based on finite element coupled cohesive element method can evaluate the fiber-optic strain evolution status during fracture initiation and propagation, and judge the initiation and propagation status of hydraulic fractures based on the strain evolution of optical fibers during on-site fracturing construction.

CRediT authorship contribution statement

Su Wang: Writing – review & editing, Writing – original draft, Methodology, Investigation, Conceptualization. **Mian Chen:** Writing – review & editing, Methodology, Conceptualization. **Jia-Xin Lv:** Writing – review & editing, Validation. **Kun-Peng Zhang:** Writing – review & editing. **Ya-Long Hao:** Writing – review & editing. **Bo-Wen Yao:** Writing – review & editing.

Declaration of competing interest

The authors declare that they have no known competing financial interests or personal relationships that could have appeared to influence the work reported in this paper.

Acknowledgments

The authors are grateful for the financial support by National Natural Science Foundation of China (No. 52334001).

References

Bessa, F., Jerath, K., Ginn, C., et al., 2021. Subsurface characterization of hydraulic fracture test site-2 (HFTS-2), Delaware Basin. In: SPE/AAPG/SEG Unconventional Resources Technology Conference. https://doi.org/10.15530/urtec-2021-5243.

Bourne, S., Hindriks, K., Savitski, A.A., et al., 2021. Inference of induced fracture geometries using fiber-optic distributed strain sensing in hydraulic fracture test site 2. In: SPE/AAPG/SEG Unconventional Resources Technology Conference. https://doi.org/10.15530/urtec-2021-5472.

Chang, Z., Hou, B., 2023. Numerical simulation on fractured shale oil reservoirs multi-cluster fracturing under inter-well and inter-cluster stress interferences. Rock Mech. Rock Eng. 56 (3), 1909–1925. https://doi.org/10.1007/s00603-022-03145-7.

Chang, Z., Hou, B., Ding, J.H., 2022. Competitive propagation simulation of multi-clustered fracturing in a fractured shale oil reservoir. Geomechanics and Geophysics for Geo-Energy and Geo-Resources 8 (3), 1–19. https://doi.org/10.1007/s40948-022-00399-x.

Chen, M., Guo, T.K., Xu, Y., et al., 2022. Evolution mechanism of optical fiber strain induced by multi-fracture growth during fracturing in horizontal wells. Petrol. Explor. Dev. 49 (1), 1–11. https://doi.org/10.11698/PED.2022.01.17.

Ciezobka, J., 2021. Overview of hydraulic fracturing test site 2 in the Permian Delaware Basin (HFTS-2). In: Unconventional Resources Technology Conference (URTeC). https://doi.org/10.15530/urtec-2021-5514.

Cippolla, C.L., Wright, C.A., 2002. Diagnostic techniques to understand hydraulic fracturing: what? Why? And How? SPE Prod. Oper. 17 (1), 23–35. https://doi.org/10.2118/75359-PA.

De Pater, C.J., Cleary, M.P., Quinn, T.S., et al., 1994. Experimental verification of dimensional analysis for hydraulic fracturing. SPE Prod. Facil. 9 (4), 230–238. https://doi.org/10.2118/24994-PA.

Gale, J.F.W., Elliott, S.J., Rysak, B.G., et al., 2021. Fracture description of the HFTS-2 slant core, Delaware Basin, West Texas. In: Unconventional Resources Technology Conference (URTeC). https://doi.org/10.15530/urtec-2021-5175.

Hou, B., Chen, M., Zhang, B.W., et al., 2015. Propagation of multiple hydraulic fractures in fractured shale reservoir. Chin. J. Geotech. Eng. 37 (6), 1041–1046. https://doi.org/10.11779/CJGE201506010 (in Chinese).

Hou, B., Chang, Z., Fu, W.N., et al., 2019a. Fracture initiation and propagation in a deep shale gas reservoir subject to an alternating-fluid-injection hydraulic-fracturing treatment. SPE J. 24 (4), 1839–1855. https://doi.org/10.2118/195571-PA.

Hou, B., Zhang, R.X., Chen, M., et al., 2019b. Investigation on acid fracturing treatment in limestone formation based on true tri-axial experiment. Fuel 235, 473–484. https://doi.org/10.1016/j.fuel.2018.08.057.

Hou, B., Wu, A.A., Chang, Z., et al., 2021. Experimental study on vertical propagation of fractures of multi-sweet of spots shale oil reservoir. Chin. J. Geotech. Eng. 43 (7), 1322–1330. https://doi.org/10.11779/CJGE202107018 (in Chinese).

Hou, B., Chang, Z., Wu, A.A., et al., 2022a. Simulation of competitive propagation of multi-fractures on shale oil reservoir multi-clustered fracturing in Jimsar sag. Acta Pet. Sin. 43 (1), 75–90. https://doi.org/10.7623/syxb202201007 (in Chinese).

Hou, B., Zhang, Q.X., Liu, X., et al., 2022b. Integration analysis of 3D fractures network reconstruction and frac hits response in shale wells. Energy 260, 124906. https://doi.org/10.1016/j.energy.2022.124906.

Kavousi, P., Carr, T., Wilson, T., et al., 2017. Correlating distributed acoustic sensing (DAS) to natural fracture intensity for the Marcellus Shale. In: SEG Technical Program Expanded Abstracts. https://doi.org/10.1190/segam2017-17675576.1, 2017.

Lei, Q., Weng, D.W., Xiong, S.C., et al., 2021. Progress and development directions of shale oil stimulation technology of CNPC. Petrol. Explor. Dev. 48 (5), 1035–1042. https://doi.org/10.11698/PED.2021.05.15.

Lv, J.X., Hou, B., Min, J., et al., 2021. Three-dimensional in-situ stress modeling of heterogeneous reservoirs with local faults. In: ISRM International Symposium-Asian Rock Mechanics Symposium. https://doi.org/10.1088/1755-1315/861/3/032071.

Molenaar, M.M., Fidan, E., Hill, D., 2012. Real-time downhole monitoring of hydraulic fracturing treatments using fibre optic distributed temperature and acoustic sensing. In: SPE/EAGE European Unconventional Resources Conference and Exhibition. https://doi.org/10.2118/152981-MS.

Shi, L., Shi, C., Tian, Z.L., et al., 2019. Several rock mechanics problems in the development of shale gas in PetroChina. Petroleum Science Bulletin 3, 223–232. https://doi.org/10.3969/j.issn.2096-1693.2019.03.020 (in Chinese).

Sui, W.B., Liu, R.Q., Cui, K., 2021. Application and research progress of distributed optical fiber acoustic sensing monitoring for hydraulic fracturing. Scientia Sinica Technologica 51 (4), 371–387. https://doi.org/10.1360/SST-2020-0195 (in

Chinese).
Sui, W.B., Wen, C.Y., Sun, W.C., et al., 2023. Joint application of distributed optical fiber sensing technologies for hydraulic fracturing monitoring. Nat. Gas. Ind. 43 (2), 87–103. https://doi.org/10.3787/j.issn.1000-0976.2023.02.009 (in Chinese).
Ugueto, G.A., Wojtaszek, M., Huckabee, P.T., et al., 2021. An integrated view of hydraulic induced fracture geometry in hydraulic fracture test site 2. In: Unconventional Resources Technology Conference (URTeC). https://doi.org/10.15530/urtec-2021-5396.
Wang, S., Chen, M., Chang, Z., et al., 2023. Experimental study on indoor multi-cluster fracturing based on distributed fibre-optical monitoring. In: International Geomechanics Symposium. https://doi.org/10.56952/IGS-2023-0028.
Wei, S., Jin, Y., Kao, J.W., et al., 2022. Reservoir stress evolution and fracture optimization of infill wells during the drilling-fracturing-production process. Acta Pet. Sin. 43 (9), 1305–1314. https://doi.org/10.7623/syxb202209009 (in Chinese).
Wei, S., Kao, J.W., Jin, Y., et al., 2021. A discontinuous discrete fracture model for coupled flow and geomechanics based on FEM. J. Petrol. Sci. Eng. 204, 108677. https://doi.org/10.1016/j.petrol.2021.108677.
Yan, J.S., Yuan, M., Zhang, Z.H., et al., 2014. Calibration and error analysis of strain coefficient of optical fiber based on stretching device. Opto-Electronic Eng. 41 (1), 23–28. https://doi.org/10.3969/j.issn.1003-501X.2014.01.005 (in Chinese).
Zeng, L., Lyu, W.Y., Xu, X., et al., 2022. Development characteristics, formation mechanism and hydrocarbon significance of bedding fractures in typical tight sandstone and shale. Acta Pet. Sin. 43 (2), 180–191. https://doi.org/10.7623/syxb202202002 (in Chinese).
Zhang, Q.X., Hou, B., Lin, B.T., et al., 2021. Integration of discrete fracture reconstruction and dual porosity/dual permeability models for gas production analysis in a deformable fractured shale reservoir. J. Nat. Gas Sci. Eng. 93, 104028. https://doi.org/10.1016/j.jngse.2021.104028.
Zhang, Q.X., Hou, B., Chang, Z., et al., 2022. Experimental study on true triaxial hydraulic fracturing based on distributed fibre-optical monitoring. In: International Geomechanics Symposium. https://doi.org/10.56952/IGS-2022-209.